Numerical and analytical investigation on meltpool temperature of laser-based powder bed fusion of IN718

(article starts on next page)

Numerical and analytical investigation on meltpool temperature of laser-based powder bed fusion of IN718

Mahyar Khorasani [a,b,*], AmirHossein Ghasemi [c], Martin Leary [a], William O'Neil [d], Ian Gibson [b,e], Laura Cordova [f], Bernard Rolfe [b]

[a] School of Engineering, Royal Melbourne Institute of Technology, Melbourne, Victoria, Australia
[b] School of Engineering, Deakin University, Waurn Ponds, Victoria, Australia
[c] Department of Mechanical Engineering, Shahid Rajaee Teacher Training University, Tehran, Iran
[d] Institute for Manufacturing, University of Cambridge, Cambridge, UK
[e] Fraunhofer Project Centre for Complex System Engineering, Department of Design, Production and Management, University of Twente, Enschede, The Netherlands
[f] Department of Industrial and Materials Science, Chalmers University of Technology, Gothenburg, Sweden

ARTICLE INFO

ABSTRACT

Prediction of meltpool features in Laser-Based Powder Bed Fusion (LB-PBF) is a complex non-linear multiple phase dynamic problem. In this investigation, numerical simulations and analytical models are offered to predict meltpool temperature and to provide a methodology to estimate melt track quality. By determining the meltpool temperature, different rheological phenomena including recoil pressure can be controlled. Recoil pressure is known to drive the keyhole and conduction modes in LB-PBF which is an important factor to qualify the melt track. A numerical simulation was carried out using Discrete Element Method (DEM) with a range of process parameters and absorptivity ratios; allowing observation of the variation of meltpool temperature and free surface morphology, as calculated by the volume-of-fluid (VOF) method. A spatially thermophysical-based analytical model is developed to estimate meltpool temperature, based on LB-PBF process parameters and thermophysical properties of the material. These results are compared with experimentally observed meltpool depth for IN718 specimens and found to have a good accuracy. The numerical and analytic results show good agreement in the conduction mode to estimate the meltpool temperature and related phenomena such as recoil pressure to control the melt track and layering quality. The analytical model does not accurately predict the keyhole mode which may be explained by evaporation of chemical elements in the examined material.

© 2021 The Authors. Published by Elsevier Ltd.
This is an open access article under the CC BY license (http://creativecommons.org/licenses/by/4.0/)

1. Introduction

Laser-Based Powder Bed Fusion (LB-PBF) is one of seven processes of Additive Manufacturing (AM) described by Gibson et al. in 2014 [1] and classified by ASTM/ISO 52,900 in the following year [2]. In LB-PBF, understanding the complexity of the meltpool dynamic is one of the main challenges for accurate result prediction. In this complex process, a process parameter set that is optimised for a specific material might not necessarily be suitable for other materials.

The dynamic meltpool behaviour in LB-PBF is a complex phenomenon that is very sensitive to the associated process parameters. As energy density exceeds a certain threshold material is vaporized and a high recoil pressure is produced that increases the tendency for keyhole formation [3-5]. On the other hand, insufficient energy density results in lack of fusion and porous, low-density components. Shrestha et al. [6] numerically simulated keyhole formation in LB-PBF by the Discrete Element Method (DEM) and showed that the keyhole size increases with higher energy density and local temperature. They [7] also investigated the combination of experimental and numerical methods by 3D power scale model using the Volume of Fluid (VOF) in single tracks. Results showed that this method has a good agreement with experimental outcomes.

A thermal-mechanical-fluid model was used by Wang and Zou [8] to analyse the micro-scale dynamic evolution of Ti-6Al-4 V. They suggested that the temperature distribution of the meltpool can be controlled by adjusting the laser power, scan speed and hatch spacing. Queva et al. [9] used a Finite Element Method (FEM) level-set model at mesoscopic scale to examine meltpool evolution and track development in LB-PBF of Inconel 718 and Ti-6Al-4 V. They utilized volumetric and surface models for laser/powder and laser/substrate interactions. This study showed both recoil pressure and vaporisation drive capillarity and affect temperature field evolution and meltpool features. The model also showed good flexibility for describing both Inconel 718 and Ti-6Al-4V. Wu et al. [10] developed a numerical model to discuss the relationship between surface morphology and process parameters. They found that the volume fraction of the meltpool and associated lifetime (the time that liquid phase is presented) directly drives the surface morphology. The optimum values of these two factors produce the best surface quality in LB-PBF of Ti-6Al-4 V. Another model that is used for simulating heat transfer and meltpool fluid dynamic behaviour is a 3D VoF. This model is coupled with a sequential powder addition algorithm to obtain random powder distribution. The molten metal flow and free surface formation were simulated by this method and found good agreement with the experimental results [11]. King et al. [12] studied the effect of recoil pressure and Marangoni's convection in LB-PBF with a high fidelity powder-scale model. They introduced pore formation mechanisms at the edge of scan tracks and suggest a series of solutions to pore mitigation. King et al. [13] also studied the keyhole and conduction modes in LB-PBF of metals by simulating the meltpool and powder interaction. They showed that the laser power, scan speed and beam diameter drive the threshold transition from conduction mode to keyhole mode. The threshold can be used to identify the optimum range of laser power, speed and beam size. A thermomechanical model was presented by King's group [14] to simulate the LB-PBF of Ti-6Al-4V to analyse the residual elastic strain. The results of the simulation were validated by synchrotron X-ray diffraction with good accuracy. The investigation showed the modest strain happened in island scans compared to continuous scan patterns. The method also showed the difference between the simulation and experimental results. This can be related to material properties, effective absorptivity and layer and beam agglomeration method.

Tapia et al. [15] worked on a Gaussian Process-based Surrogate (GPS) model of a metal LB-PBF process that predicts meltpool depth in a single track. The GPS model was validated by ten cross-validations and the results showed a high degree of confidence in meltpool depth. This study also showed faster process time to obtain the results compared to the existing models. King et al. [16] also offered the Diablo code-based model to demonstrate a mitigation strategy for dross formation in the overhang area in LB-PBF. The proposed model showed that the surface tension binds melted particles and increases the contact with the build plate to produce smooth melt tracks and better heat transfer. Cook and Murphy [17] provided a comprehensive review on meltpool simulation and presented the overall status of the meltpool simulation in the literature. They reported that due to the complexity of the physics of the meltpool, several important problems need to be solved to provide a more accurate simulation process. These include the absorption of heat source and powder, the sensitivity of the predictions, validation, in-situ time resolve measurement of meltpool temperature and linking the presented simulation to residual stress and mechanical properties.

Most of the presented literature are related to the meltpool geometry and mechanical properties of the manufactured specimens. Many current simulations are neglecting the effect of convection between shielding gas and the meltpool or simulate the LB-PBF process on a solid bed rather than a powder bed. Therefore, a powder bed and real simulation is useful to correctly verify the analytical developed model based on thermophysical properties of the material to estimate meltpool temperature and subsequentl rheological aspects of the meltpool.

In the current study, the analytical model, which works based on thermophysical properties of the feedstock is developed to predict the meltpool temperature. Different process parameters and absorptivity ratios were applied to both analytical and numerical models to simulate the conduction and keyhole modes in LB-PBF. The presented model was verified with the numerical simulation and different phenomena that occur in different temperature ranges were discussed and governing mechanisms explained.

2. Limitations of in-situ meltpool temperature measurement

There are a number of limitations for in-situ meltpool temperature measurement. For meltpool temperature below 1000 °C the emitted light energy from the meltpool is relatively low, and is challenging to capture with conventional silicon-based image sensors. Non-silicon sensors such as Indium Gallium Arsenide (InGaAs) have been proposed as a technology to resolve this problem; however, these sensors may have a lower associated frame rate. Another potential limitation of thermal cameras is the high number of photons that result from higher temperature of meltpool due to Planck's law. These scenarios can produce measurement errors, especially when quantifying the transition from conduction mode to keyhole mode. In thermal cameras, the received photons are converted to electrons and then stored in memory. The penetration depth of the sensor limits the number of stored electrons and potentially causes error in measurement. If a relatively short exposure time is selected then sensor noise is dominant and these measurement errors increase. Generally, for high-speed cameras, the maximum and minimum detectable signals are in the range of 60 dB, which can only detect the temperature in the range of 1500–5000 K. The acquired high-speed camera data is initially stored in short-term memory which is then transferred to permanent computer storage. Consequently, the continuous data that can be acquired is limited by the associated storage capacity and data transfer rates.

In keyhole mode, the meltpool can be obscured by the plume, and ejected particles. The plume is invisible inside of the meltpool and attenuates the heat signals and can therefore cause an incorrect reading. In addition, the meniscus on the surface of the meltpool deviates the reflected light from the surface that increases the chance of error. These limitations make analytical and numerical models necessary to estimate meltpool temperature which is more cost-effective and faster for research and development with acceptable accuracy.

3. Analytical model to calculate the meltpool temperature

In LB-PBF, the induced energy, E_d, and meltpool temperature is a function of process parameters. Eq. (1) quantifies the induced energy density is related to absorption coefficient, η, laser power, L_p, scan speed, S_s, and beam area, B_a [1].

$$E_d = \frac{\eta L_p}{S_s B_a} \tag{1}$$

The absorption coefficient, η, is one of the physical properties of the material. The energy density is consumed to increase the temperature and enthalpy to melt the powder particles and to form the melt region. The enthalpy of Inconel 718 is a function of temperature in a solid phase, solid-liquid and the liquid phases (melting).

Thus, Eq. (2) quantifies the relationship between meltpool peak temperature versus thermophysical material properties, including:

Table 1
Material properties of Inconel 718.

Property	Symbol	Value	Unit	Ref
Reflection coefficient	R	0.7		[18]
Solidus temperature	T_s	1493	K	[19]
Liquidous temperature	T_m	1609	K	[19]
Boiling temperature	T_v	3186	K	[19]
Heat capacity of solid phase	C_{ps}	Fig. 1	$kg.m^{-3}$	[19]
Heat capacity of liquid phase	C_{pm}	Fig. 1	$kg.m^{-3}$	[19]
Density of solid phase	ρ_s	Fig. 2	$J.kg^{-1}.K^{-1}$	[19]
Density of liquid phase	ρ_m	Fig. 2	$J.kg^{-1}.K^{-1}$	[19]
Latent heat of fusion	L_f	270	$kJ.kg^{-1}$	[19]
Latent heat of vaporisation	L_V	6300	$kJ.kg^{-1}$	[19]
Surface tension coefficient	γ	1.89	$N.m^{-1}$	[19]
Marangoni coefficient	$\partial\gamma/\partial T$	-1.1×10^{-4}	$N.m^{-1}.K^{-1}$	[19]

$$C_p = 0.21624 + ((1.24323\times10^{-3})\times T) - ((2.26426\times10^{-6})\times T^2) + ((2.00584\times10^{-9})\times T^3) - ((6.16396\times10^{-13})\times T^4)$$
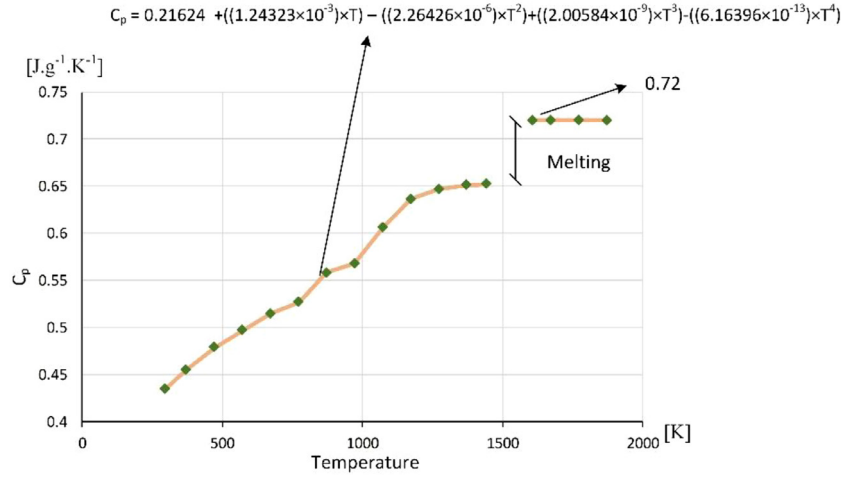
Fig. 1. Specific heat capacity versus temperature for Inconel 718 [19].

initial temperature, T_0, solidus temperature, T_s, liquidous temperature, T_m, phase transformation enthalpy, ΔH_m, and heat capacity in solid-state, C_{ps}, and liquid state, C_{pm}, respectively. These factors are independent parameters and meltpool temperature, T_{mp}, is a dependant parameter that needs to be calculated. The thermophysical properties of Inconel 718 are shown in Table 1.

$$E_d = \int_{T_0}^{T_s} C_{ps}dT + \Delta H_m + \int_{T_m}^{T_{mp}} C_{pm}dT \tag{2}$$

Fig. 1 shows the specific heat has a different trend in different phases so to obtain the relation of the specific heat versus temperature, the polynomial regression was applied that is shown in Eq. (3).
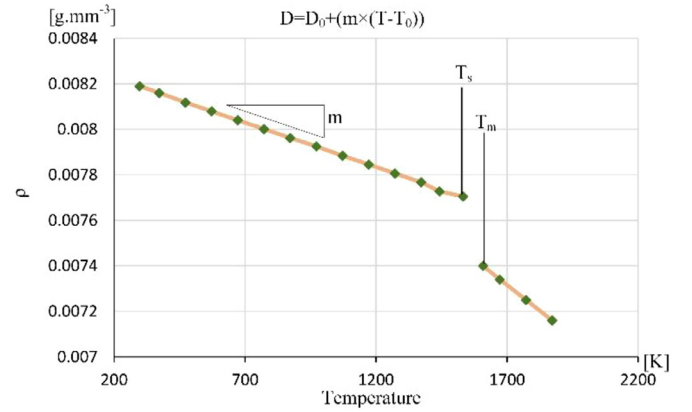
$$C_{ps} = 0.21624 + 1.24323 \times 10^{-3} \times T - \left(2.26424 \times 10^{-6}T^2\right)$$
$$+ \left(2.00584 \times 10^{-9} \times T^3\right) - \left(6.16396 \times 10^{-13} \times T^4\right),$$
$$for \; T = 298\,K - 1493\,K \tag{3}$$

$$C_{pm} = 0.72 \; \frac{J}{g^\circ K} \quad for \; T \geq 1609\,K$$

$$\Delta H_m = 270\frac{J}{g}$$

Eq. (2) reports the gravimetric energy density; therefore, density must be multiplied by enthalpy. The density of the metal is a function of temperature as identified in Fig. 2 for Inconel 718. To

Fig. 2. density versus temperature relationship for Inconel 718 [19].

obtain the value of density in each phase a regression analysis has been carried out and is quantified in Eq. 4(a) and 4(b):

$$\rho_s = \left(8.19 \times 10^{-3}\right) + \left[\left(-3.93 \times 10^{-7}\right) \times (T - 298)\right] \tag{4a}$$

$$\rho_m = \left(7.40 \times 10^{-3}\right) + \left[\left(-9.09 \times 10^{-7}\right) \times (T - 1609)\right] \tag{4b}$$

When heating Inconel 718 in the range of 1493–1609 K, the material undergoes an endothermic phase transformation with the as-

Table 2
Process parameters for Test Cases 1 to 10.

Test Case	Laser Power [W]	Scan Speed [mm/s]	Absorption ratio
1, 6	225	1060	0.16, 0.32
2, 7	255	960	0.16, 0.32
3, 8	255	860	0.16,0.32
4, 9	285	760	0.16,0.32
5, 10	315	760	0.16,0.32

sociated energy density being defined by Eq. (5).

$$E_d = \int_{T_0}^{T_s=1493} C_{p_s} dT + \Delta H_m + \int_{T_m=1609}^{T_{mp}} C_{p_m} dT \tag{5}$$

Eq. (5) may then be solved in terms of meltpool temperature, T_{mp}:

$$T_{mp} = \frac{E_d - \left(\int_{T_0}^{1493} C_{p_s} dT + \Delta H_m \right) + (C_{p_m} \times 1609)}{C_{p_m}} \tag{6}$$

In LB-PBF, laser power, scanning speed, beam area and preheating temperature, (T_0), are adjustable process parameters while absorption ratio, specific heat capacity, latent heat of fusion, and critical temperature are the thermophysical properties of the material.

Decreasing laser power and preheat temperature decrease the meltpool peak temperature while scanning speed and beam diameter have a reverse relationship with meltpool temperature. Different ranges of laser power, scan speed and two levels for absorptivity were selected for this experiment to simulate both conduction and keyhole modes. These process parameters were selected in such a way that produces different meltpool temperature based on the presented analytical model. Table 2 shows the process parameters for each identified Test Case.

4. Numerical model to calculate the meltpool peak temperature

The numerical simulation of meltpool temperature is computationally and technically challenging and is subject to considerable uncertainty in fundamental meltpool dynamics, stability and related defects. In response to this complexity, and to robust simulation outcomes, state-of-the-art Computational Fluid Dynamics (CFD) tools[1] were applied that model free-surface fluid flow and multiphase heat transfer with solidification morphology; simulations accommodate multiphysics interactions in micro and mesoscale. The computational tool has LB-PBF relevant aspects such as transient heat source; dynamic powder spreading and packing and the related equations are presented in the Appendix (Tables A1 to A7). The other items considered in the simulation are, laser and particle interactions; transient meltpool dynamics and nonlinear material response. These simulation capabilities enable best-practice research outcomes as validated for LB-PBF applications [20-24]. The following sections describe the simulation attributes associated with: heat source modelling; powder particle distribution; model geometry and boundary conditions; the discrete element method; and, material properties.

4.1. The heat source model

Various heating models are presented in the literature to accommodate the laser beam heating and melting of the LB-PBF powder bed [1, 25-27]. When the energy density of the laser beam exceeds a certain value, the material in the region of the centre of the meltpool is evaporated, resulting in *keyhole mode,* where the

laser energy penetrates deeply through a keyhole/cone shape into the material [28]. The energy of the heat source in keyhole mode is absorbed by both the lateral surfaces and bottom of the meltpool. Conversely, if the LB-PBF energy density is at a relatively low level, the powder particles are melted, but no evaporation occurs. In this situation the laser energy is absorbed by the upper surface of the powdered material, referred to as *conduction mode* [29].

In this research a Gaussian distribution model is used to characterise the heat dispersion for both conduction and keyhole modes.

For the conduction mode, a surface heat source model applied that has heat flow into the upper powder bed surface. For keyhole mode, a body heat source model with volumetric energy density is used [1, 30] for the numerical simulation. Eqs. (7) and 8 define the surface, q_s, and body, q_b, heat source models in terms of laser power, P, absorptivity by the upper surface, e_1, and body, e_2, laser beam parameters: radius of the beam at the upper surface of the powder, r_1, radius of the laser at the end of the meltpool, r_2, and the depth of heat source, h. In this experiment r_1 is set to beam diameter (r_1=50 μm) and r_2 is estimated by the numerical model based on the calculated depth of the penetration and r_1.

$$q_s(x, y) = \frac{3Pe_1}{\pi r_1^2} e^{\left[\frac{-3(x^2+y^2)}{r_1^2} \right]} \tag{7}$$

$$q_b(x, y, z) = \frac{3Pe_2}{\pi (1 - e^{-3}) h r_2^2} e^{\left[\frac{-3(x^2+y^2)}{r_2^2} \right]} \tag{8}$$

To investigate both conduction and keyhole modes, a range of scan speeds, laser powers and absorptivity ratios were selected (Table 2). In LB-PBF, estimating the appropriate value of absorptivity is a complex task and is dependant on various factors such as the thermophysical and electrical properties of the material; surface quality; and laser parameters, including power, speed and wavelength. Therefore, it is a common practice to use an empirical absorption coefficient. In this model, to verify the simulation results each test was simulated by two values of an absorption ratio including 0.16 and 0.32 [31]. This provides the possibility to simulate both conductive and keyhole modes.

4.2. Powder particle distribution

Fig. 3 shows the geometry model and associated meshing. The geometry model consists of two sections including the base metal and powder bed. The LB-PBF simulation tool was used to model the powder bed with a total number of mass particles of 50,000 (Based on the area of the substrate) with five different particle sizes comprising 10, 12.5, 15, 17.5, 20 μm.

4.3. Geometry of the model and boundary condition

The mesh size was selected at 5 μm to provide a balance between simulation efficiency and resolution ratio of powder evolution. The lateral powder boundary conditions (Y-coordinates and negative X-direction) was selected as "wall" to prevent powder movement. In the positive X-direction the boundary condition allows powder movement in a single direction (along with laser movement) to simulate an "outflow" environment. In this simulation, gravitational attraction is simulated in the negative Z-coordinate and powder particles are compactly distributed by the recoater blade and the upper powder layers are free to move above each sublayer with the same X- and Y-coordinates. Thus, this method simulates the actual powder bed distribution and enables the evolution of the powder distributions subject to a range of process parameter Test Cases (Table 2).

---

[1] Flow Science, Inc., Santa Fe, NM, USA. FLOW-3D Version 11.2 (2019).
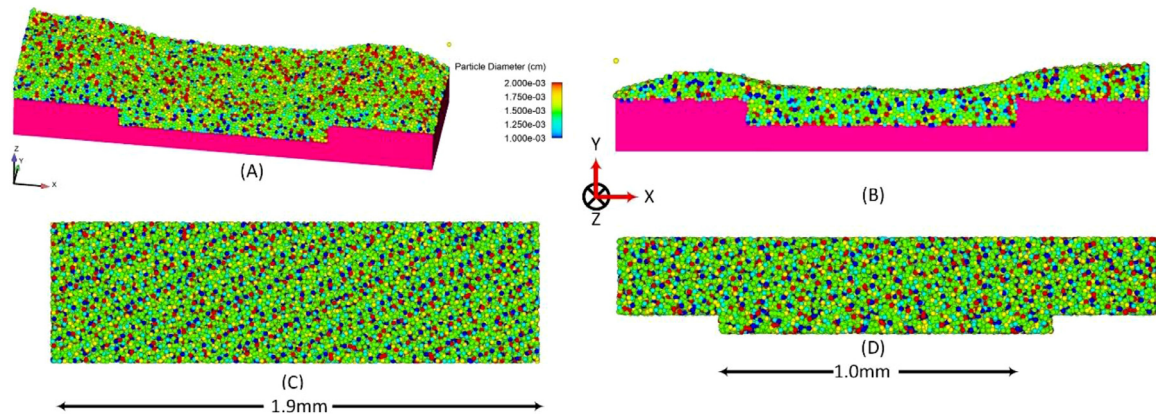
Fig. 3. Geometry of the powder bed and meshing showing (A) isometric view of entire geometry model (B) side elevation of meshed geometry model (C) plan view of powder bed (D) side elevation of powder bed.

Heat exchange between the shielding environment and the surfaces of the geometry is defined. In particle separation, two interactions including particle-particle and particle-mesh walls are enabled. As the powder particles settle in the solid bed, they accumulate in the positive Z-direction and the interaction of powder particles and build platform determines the powder packing density. This factor is definable in the simulation tool that was selected proportional to the particle sizes. In real conditions, the powder packing density is associated with different factors such as recoater type and solid bed size, shape and speed. In this simulation, a distance of 30 µm was maintained between recoater and powder bed for the mentioned particle size and to obtain suitable separation[2] and packing density.

4.4. Discrete element method

The LB-PBF build procedure requires the simulation of the powder bed because the simulation condition is different compared to printing on a fully solid substrate. In this simulation to obtain greater accuracy, powder particles must be considered as there are multiple reflections of the laser beam through the particles. Flow3D uses the Discrete Element Method (DEM) to numerically simulate the behaviour of discrete interacting bodies. Thus, it is an ideal tool for simulation of powder bed systems. The distribution of the powder diameter was selected in the range of 10–30 µm and discretised to the percentage of mass distribution. In this simulation, an explicit time integration for the small particles was used. A time-step, Δt, that satisfies the Rayleigh criteria may be defined by Eq. (9); based on the minimum radius of powder particles (R_{min}= 10 µm); Modulus of elasticity, E; scan speed, v; and, density of the powder, ρ [32]:

$$\Delta t = \frac{\pi R_{min}\sqrt{\rho/E}}{0.163v + 0.877} \tag{9}$$

In the current experiment, all particles are identified by the diameter, mass, velocity and momentum; therefore, it is possible to track individual powder particle trajectories.

4.5. Material properties

The thermophysical properties of Inconel 718 (Table 1, Figs. 1 and 2) required to simulate meltpool phenomena include material density, viscosity, specific heat, and thermal conductivity. These properties are a function of temperature as required.
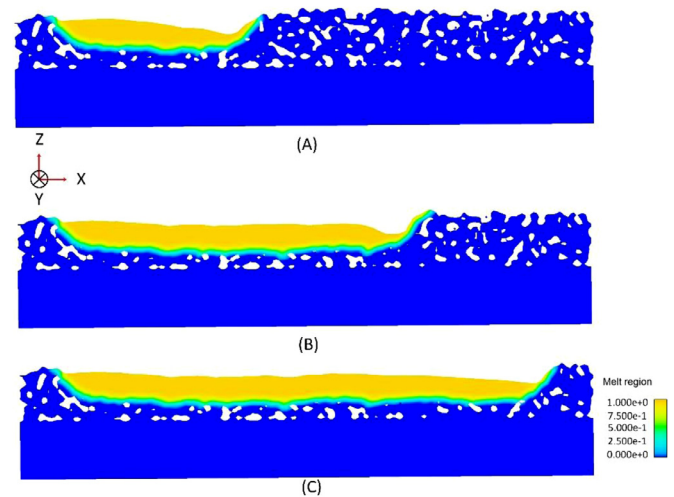
Fig. 4. The formation of meltpool in test case 2 for (A) 300µs (B) 600µs and (C) 900µs.

5. Results and discussion

5.1. Single-Layer simulation

In LB-PBF when the laser irradiates the powder bed, the temperature of powder increases. Since the Gaussian beam is used for the simulation, the temperature at the centre region of the irradiation zone has the highest value. With further increase in the temperature, powder particles from the centre region start to melt, with this molten zone radiating outwards. In this situation, smaller particles melt more rapidly than do larger particles and the meltpool flows and fills the gaps between particles. When the laser beam passes through the powder particles, solidification begins and forms a single track. Fig. 4 shows the movement of the meltpool from left to right and the formation of the single track meltpool.

Based on the selected process parameters and absorptivity, two well-known modes occur in LB-PBF including conduction mode and keyhole mode. This classification is based on two typical heat transfer modes comprising conduction and convection [13, 33, 34]. In the conduction mode, the conduction phenomenon transfers the heat from the surface to the body of the laser track and forms shallow weld nuggets. In keyhole mode, the heat is transferred to the body of the meltpool by conduction and radiation. In this simu-

---

[2] Where separation is defined as powder distribution on the substrate.

Table 3
Different speed to power ratios and calculated meltpool temperature for absorptivity 0.16.

Test Case	Laser Power (LP) [W]	Scan Speed (SS) [mm/s]	LP/SS [J/mm]	Peak Temperature by Analytical model [K]	$\frac{E_d}{\Delta H_m}[\frac{g}{m^3}]$
1	225	1060	0.212	1082	6.01
2	255	960	0.266	1293	7.52
3	255	860	0.297	1415	8.39
4	285	760	0.375	1725	10.62
5	315	760	0.414	1881	11.73

lation, 10 Test Cases were examined. The first five Test Cases are set for conduction mode and the second five Test Cases are set for keyhole mode (Table 2).

5.2. Effect of process parameters on meltpool temperature

LB-PBF is a heat-driven process which is controlled by process parameters such as laser power and scan speed that determine the energy flux to the powder particles that ultimately dictate the thermal response and melt flow. Increasing laser power transfers greater heat to the powder bed according to Eqs. (6) and 7. By increasing the amount of heat, the temperature of the material increases from the solidus point until sintering occurs. Further increase in laser power raises the temperature to the melting point and if the temperature continues to rise, evaporation will occur and recoil pressure drives the meltpool related features.

Considering Eq. (10), laser power, L_p, and scan speed, S_s, are governing design factors dictating the overall temperature and thermodynamics of the meltpool.

$$T_{mp} = \frac{\eta L_P - S_S B_A \left(\int_{T_0}^{1633} C_{p_s} dT + \Delta H_m \right) + (C_{p_m} \times 1683)}{S_S B_A C_{p_m}} \qquad (10)$$

In this simulation, a range of laser power to scan speed ratios were tested with the analytical and numerical models as shown in Table 3. When using the smallest laser power to scan speed ratio (Test Cases 1–3) the meltpool temperature cannot reach the material melting point (1533 K) and therefore cannot melt the powder bed as shown in Fig. 5 (A-I). The laser track observation in these figures shows that the elevated temperature for Test Case 1, 2 and 3 is 1087 K, 1364 K and 1471 K respectively. Table 3 and Fig. 5 prove that the analytical model provides robust estimates for elevated temperatures below the melting point. and Test Cases 4 and 5 with fully melting and liquid flow in conduction mode.

Fig. 6 shows that for Test Cases 1–3 a shallow meltpool is formed in the thickness range of <40 μm. This meltpool depth is insufficient to melt the powder within the full layer thickness (set to 100 μm in this simulation) and consequently results in a lack of fusion defect. (Note, the white area in the figures shows distance between powder particles).

When the ratio of laser power to scan speed (Test Cases 4 and 5) increases, higher heat is induced in the laser track which forms the complete meltpool as shown in Fig. 5 (J-O). In this situation, the powder bed is melted and the depth of the meltpool increases to 60 μm, which shows a weak bonding to the solid bed (substrate) as shown in Fig. 7. When considering the higher laser power to scan speed, commonly the movement of fluid in the meltpool is equally slower. In this dynamic situation, two processes occur, firstly the fluid moves out from the centre of the laser track carrying heat, which can enhance heat transfer. Secondly, fluid in the outer regions which experiences zero velocity accelerates and fills all gaps in the powder particles to form a complete meltpool [35]. Simultaneously, due to the Marangoni effect, convection transfers heat from the bottom of the laser penetration depth to the surface and then outward, generating a larger width, 'cone-shape' meltpool that increases meltpool depth as is shown in Fig. 7.

By reducing scan speed, the cooling rate and viscosity decrease, which in turn increases the meltpool flow. Subsequently, the Reynolds number increases, resulting in higher turbulence within the meltpool, thereby the melted material flows and fills all gaps in a powder bed (Fig. 7B), which causes high penetration depth and good bonding. This can reduce defects and improve mechanical properties. Fig. 8 shows the line plot for melt track temperature for Test Cases 1 to 5. As illustrated in this figure the simulated analyses are found to have a good accuracy agreement with the analytical model for the first five test cases.

Fig. 9 shows the calculated meltpool temperature by the proposed analytical model versus the simulated results. As can be seen in this figure, the proposed analytical model "which works based on the thermophysical properties of the materials" has good accuracy and can be used to define appropriate process windows before starting the experiments. This can significantly reduce the cost and time of the production, especially for new material where no processing data is available.

5.3. The effect of high absorptivity on the meltpool temperature

In the keyhole mode or penetration mode, a cone shape laser penetration has shaped on account of higher laser power to scan speed ratio or absorptivity of the material. The cone shape heat source or keyhole is characterized by a deep narrow weld, which is formed due to the evaporation of metal. The energy of the heat source is absorbed by the wall of the keyhole/cone shape and transferred to the metal that can produce a deeper meltpool with more flowability [26, 36]. As shown in Table 4, Test Cases 6–10 were set for higher absorptivity (η=0.32). In this case, the test cases are in keyhole mode which shows higher energy absorption and temperature. Table 4 shows that higher meltpool temperature was obtained from the analytical model compared to the conduction mode presented in Table 3.

Most of the numerical methods for keyhole mode laser processing involve simplifying assumptions. The recoil force, the surface tension pressure, and hydrostatic liquid pressure are commonly assumed to be balanced. Also, many current models consider heat transfer by conduction only, and convection is not taken into account; this idealisation may limit the range of predictability of these models and reduce the accuracy of the results [37].

To determine the performance of the proposed analytical model, Test Cases 6–10 were simulated by Flow3D Version 11.2. Fig. 10 (A-F) shows for Test Case 6 and 7, complete meltpool track is formed and the powder bed is fully melted due to the high temperature of the LB-PBF process. The fully melted track is also found by the analytical model shown in Table 4. For Test Case 6 and 7, the numerical simulation of the laser track temperature was obtained as 1920.94 K and 2342.88 K respectively. Fig. 11 shows in Test Cases 6 and 7 the calculated meltpool temperature for the analytical model has 24.34% and 37.67% difference versus numerical simulation. The difference between these two models for Test Cases 8, 9 and 10 was obtained as 38.76%, 26.36% and 20.22% respectively. The largest difference between these two models in
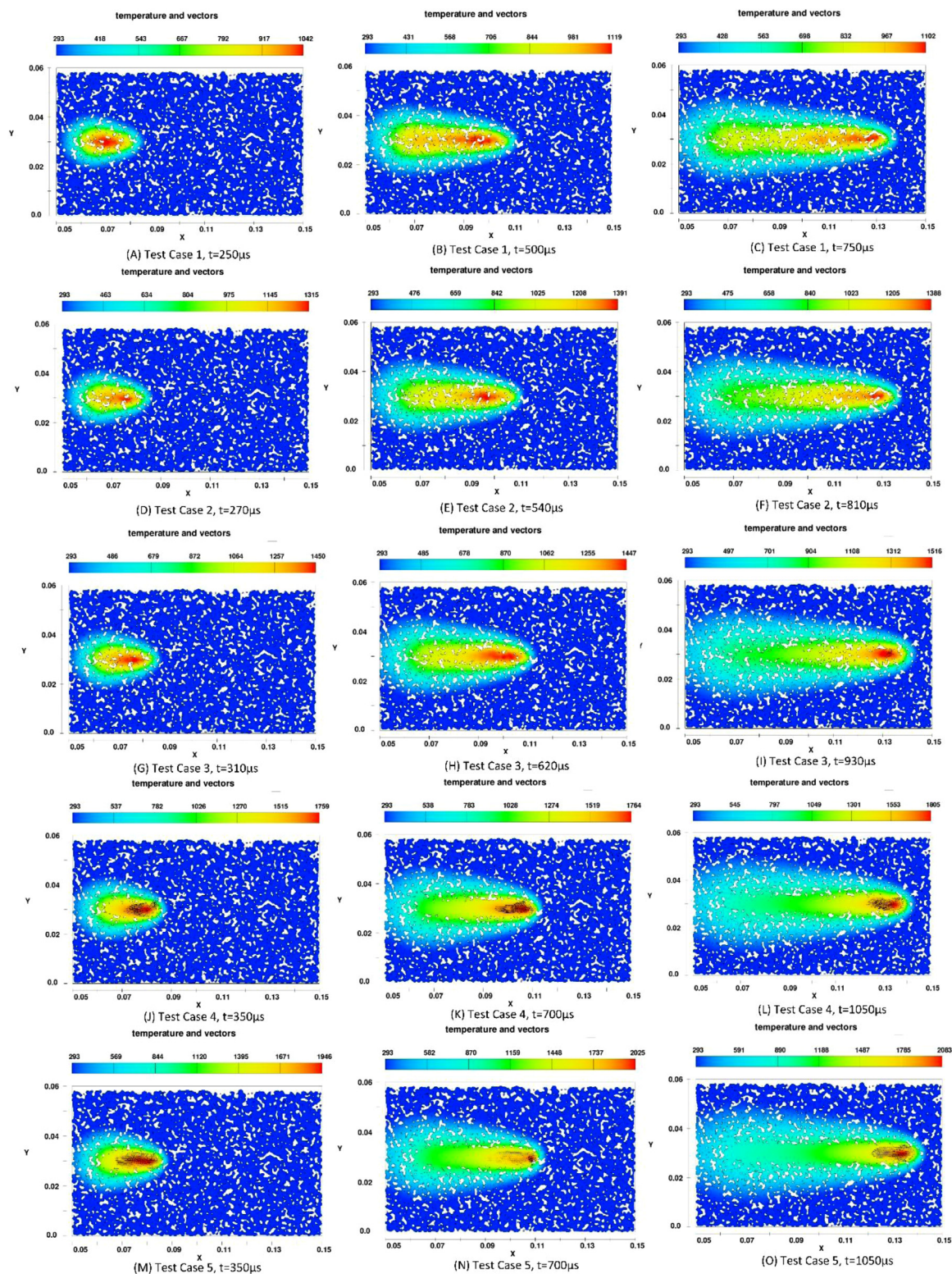
Fig. 5. Temperature field (K) of melt track for Test Cases 1–3 with no melting effect.
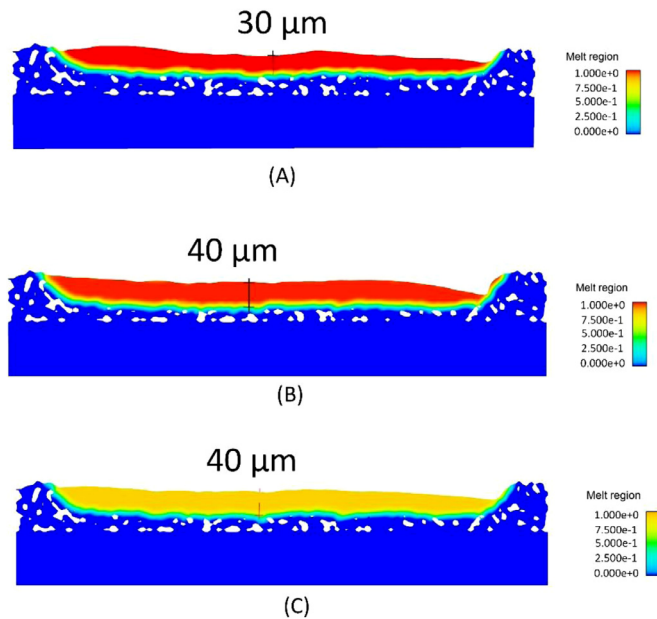
keyhole mode compared to conduction mode is related to the higher temperature, recoil pressure and evaporation of the chemical elements for Inconel 718. The recoil and evaporation pressure are not considered in the analytical model, therefore usability of this model is limited to the certain power range and energy densities.

In keyhole mode by increasing the ratio of laser power to scan speed from 0.212 to 0.266 the temperature of the meltpool increases which is shown by both analytical and numerical models. However, when increasing this ratio from 0.266 to 0.414, no significant increase in meltpool temperature was observed in the numerical model. The recoil pressure is dominant due to its exponential

Table 4
Different Speed to power ratios and calculated meltpool peak temperature for absorptivity 0.32.

Test Case	Laser Power (LP) [W]	Scan Speed (SS) [mm/s]	LP/SS	Peak Temperature by Analytical model [K]	$\frac{E_d}{\Delta H_m} [\frac{g}{m^3}]$
6	225	1060	0.212	1921	12.02
7	255	960	0.266	2343	15.04
8	255	860	0.297	2587	16.79
9	285	760	0.375	3208	21.23
10	315	760	0.414	3520	23.47

Fig. 6. The meltpool depth for laser power to scan speed. Note that meltpool depth is less than the layer thickness and may lead to a lack of fusion defect. Temperature (K) in meltpool indicated.
(A) Test Case 1, LP/SS = 0.212 J/mm (B) Test Case 2, LP/SS = 0.267 J/mm and (C)) Test Case 3, LP/SS = 0.297 J/mm.

component is positive along the sidewalls of the depression where the liquid escapes vertically due to the high vapour pressure. The depression phenomena observed in our case study is also found by King and Rai et al. [13, 38]. The deep meltpool depression in Fig. 12(C) is also related to the high temperature >4400 K and subsequently high vapour surface flux from gas plumes which exerts a pressure force and ejects liquid materials. Due to the cooling effect, two different vortixes appear close to the meltpool. The first vortex is related to the convection and conduction cooling and the second vortex appears due to Marangoni's convection. The ejected material below the laser beam forms small droplets and the interaction of gas plume recoil pressure and vortexes 1 and 2 move the particles away from the meltpool and causing it to deepen as shown in Fig. 12(C). A third vortex is also driven by cooling effect and tends to minimize surface energy.

Fig. 12(B) shows the conduction mode for Test Case 1. When the laser's hottest spot passes from the plane in "X" direction, the temperature of the depression reduces, causing an exponential reduction in recoil pressure. By this reduction in temperature, the surface tension increases, which overcomes the tendency of the recoil pressure to keep the depression open. In this condition, the melt flow direction changes to an inward direction, but cannot guarantee the complete filling of all gaps in the powder bed, thereby increases the chance of porosity as seen in Fig. 12(B).

Another reason for the identified pores in Fig. 12(B) is denudation. When the heat source passes through the powder the molten material fills the depression and the region of the fused melt track grows in height. Due to asymmetrical cooling in the transition area, a lateral liquid flow occurs. This phenomenon partially melts powder particles that are in touch with the melt track and due to Marangoni's convection, surface tension pulls the partially melted powders toward the cold spot. If the induced energy in powder bed is not high enough to melt and flow the material, then the mentioned phenomenon makes an unstable bridge between the gaps of powder particles, which can produce defects in subsequent layers [1]. The mentioned mechanism in lower induced energy on powder bed was also observed by Yadroitsev et al. [39]. These pores can be solved by selection of suitable hatch space when scanning subsequent layers.

To identify the determinant scale for keyhole and conduction modes, the induced energy density is divided by the material enthalpy at melting. This criterion has been tested for different metals such as stainless steel 316 L [12, 40] processed by LB-PBF. Our case study shows that for $E_d/\Delta H_m$ ratios greater than 12, the key-

dependence on process temperature. In this situation, the higher induced energy, the higher recoil pressure and evaporation; therefore, the temperature has an insignificant increase.

For Test Cases 8–10 the meltpool peak temperatures approach the boiling point (3005 K) and the recoil pressure applies an exponentially increasing force which is normal to the surface and accelerates the liquid away from the centre of the melt track. This produces a depression in the meltpool with a thin liquid boundary layer at the bottom and forms a noticeable topological depression.
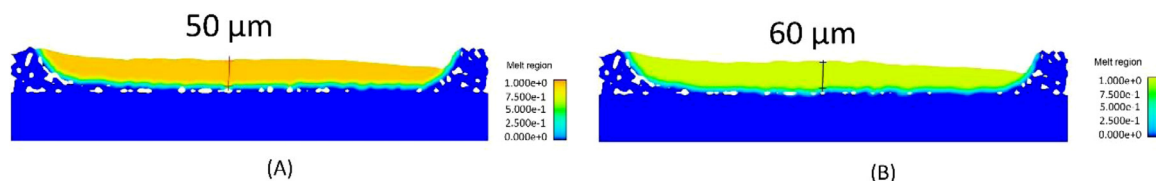
The recoil pressure is lower at the bottom of the depression (Fig. 12(A)), where the temperature has the highest value. The vertical velocity component of the melted liquid is negative at the bottom of the depression which causes the recoil force to generate a depression in the order of 120 μm. However, the vertical velocity

Fig. 7. The meltpool depth for the laser power to scan speed ratio of (A) Test Case 4, LP/SS = 0.375 and (B) Test Case 5, LP/SS = 0.414 J/mm.
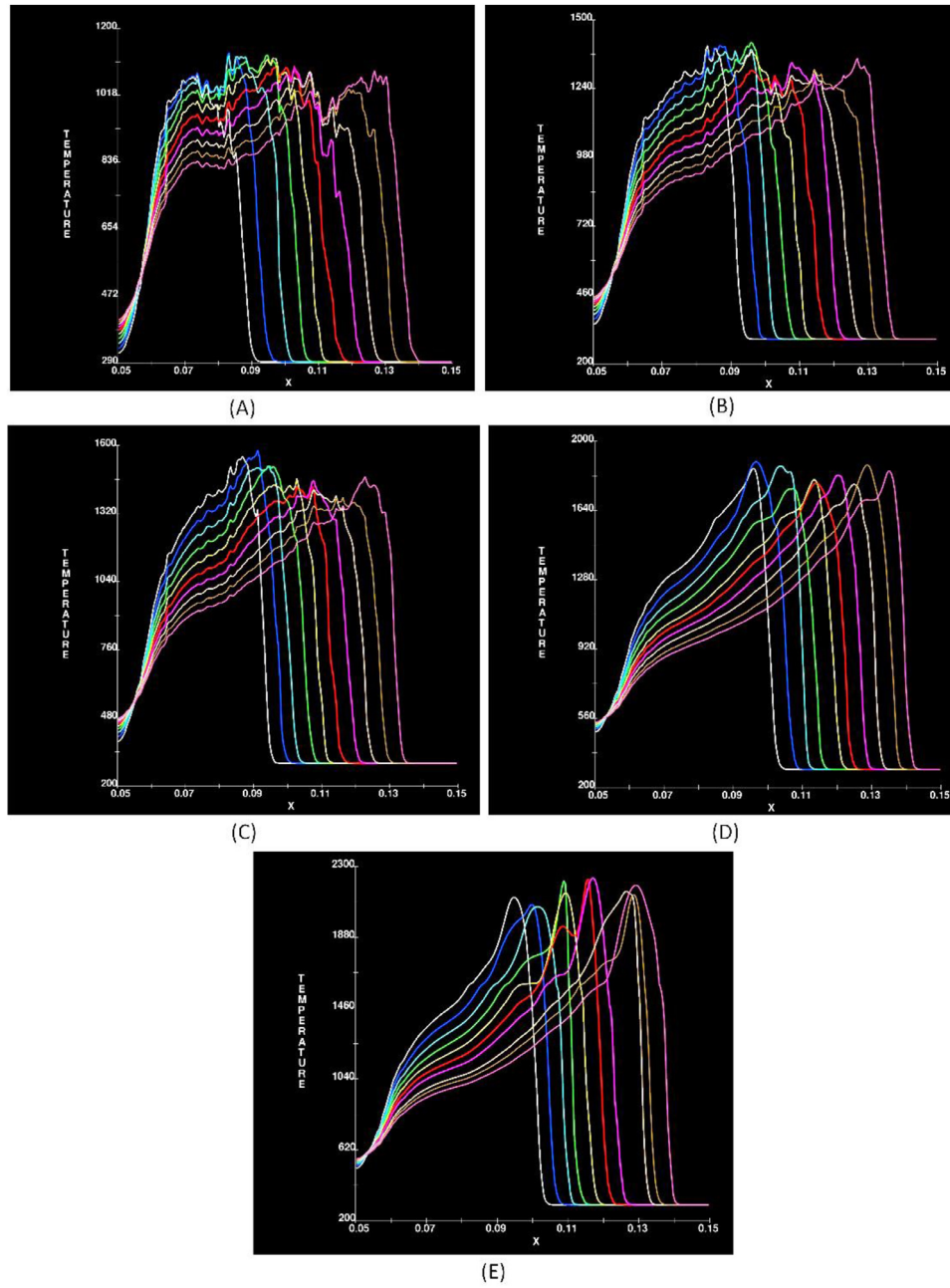
Fig. 8. One-dimensional temperature profiles (K) for Test Cases 1 to 5 (A-E) presented with 10 equal time spacing within the simulation duration.
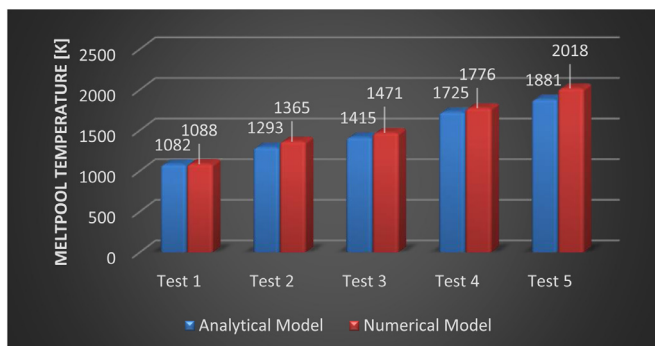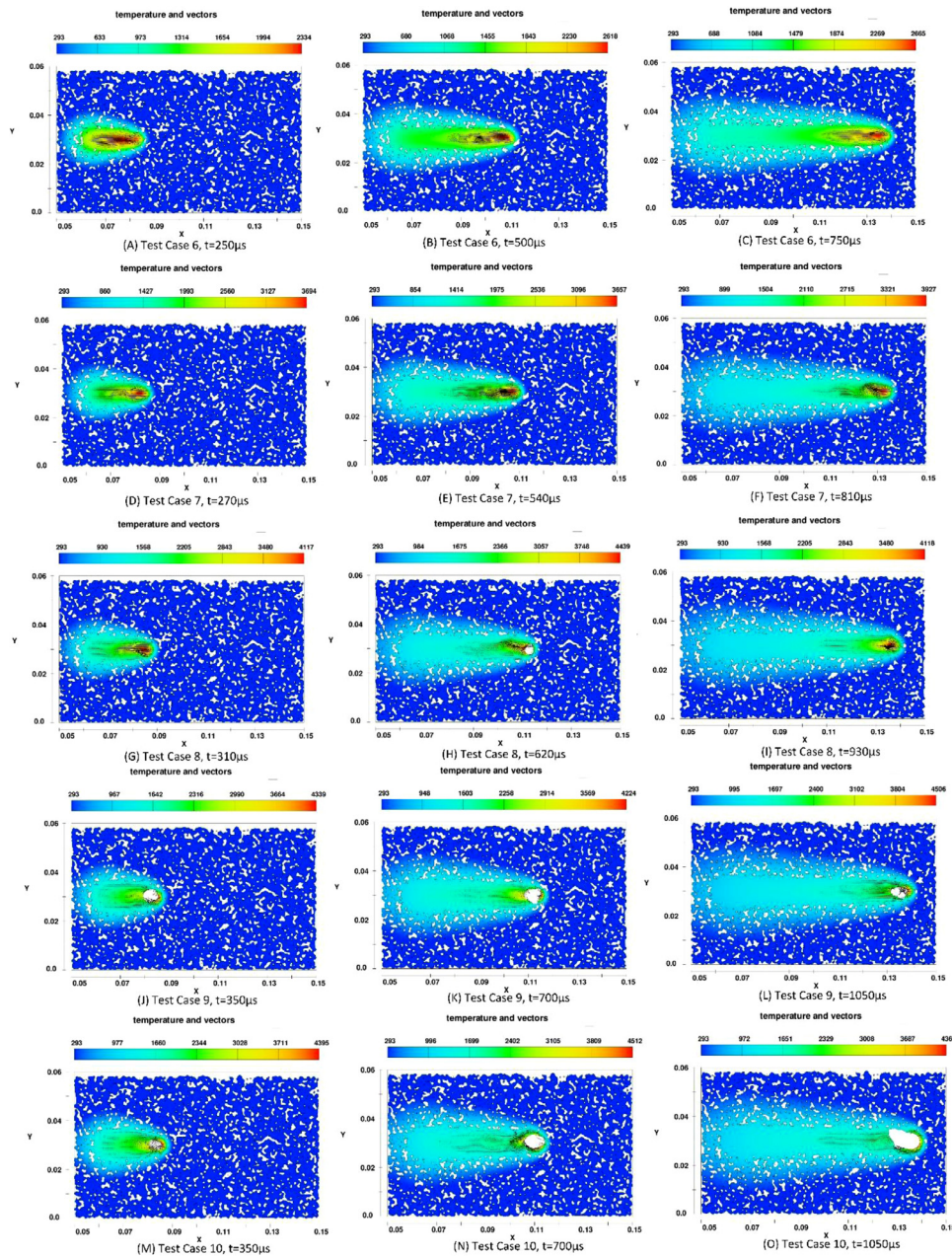

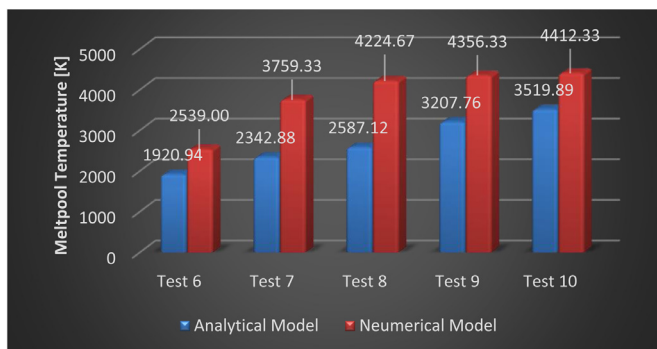**Fig. 9.** The calculated meltpool temperature versus simulated values for conduction mode.

hole mode and deep meltpool appear according to Equation 11.

$$\frac{E_d}{\Delta H_m}\{\begin{array}{l} < 12\ g/m^3\quad Conduction\ mode \\ \geq 12\ g/m^3\quad Keyhole\ mode \end{array} \tag{11}$$

Experimental validations in Section 5.4 and Fig. 12 (A and B) show that setting process parameters to produce high keyhole ratio (Test Case 10, $E_d/\Delta H_m$=23.46 g/m^3) results in the formation of a very deep meltpool which melts the solid bed, and in contrast, setting process parameters too far below this criterion (test case 1, $E_d/\Delta H_m$=6 g/m^3), the meltpool becomes very shallow which may cause bonding problem as can be seen in Fig. 5 (A-I). The meltpool depth and features showed that for Test Cases 6 to 10 the keyhole mode is dominant. Fig. 13 shows that a deep depression area is formed for Test Case 10 (which has higher induced energy and a meltpool temperature of 4400 K) at the end of the laser track

Fig. 10. (A-F) the melt track for Test Cases 6–7 with melting effect and liquid flow (G-O) melt track with fully melting condition and evaporation in keyhole mode.


Fig. 11. The calculated meltpool peak temperature versus simulated value for key-hole mode (Test Cases 6–10).

that is related to a rapid ramp down in laser power. To resolve this identified issue it is recommended to slowly ramp down the laser power.

5.4. Verification of simulated meltpools

The temperature of the meltpool has a direct relation to melt-pool depth which can produce the conduction or keyhole modes. Therefore, to verify the results of the simulation four test cases with different process parameters have been carried out and compared with the experimental tests with similar printing condition. The cross-section in Y-direction depicts the shape of the melt-pools and is shown in Fig. 14.. The simulated meltpool depth in Fig. 14 (A-B) is in conduction mode while Fig. 14 (C-D) is in key-hole mode. The maximum errors between simulated melt tracks and experimental tests for the conduction and keyhole modes were
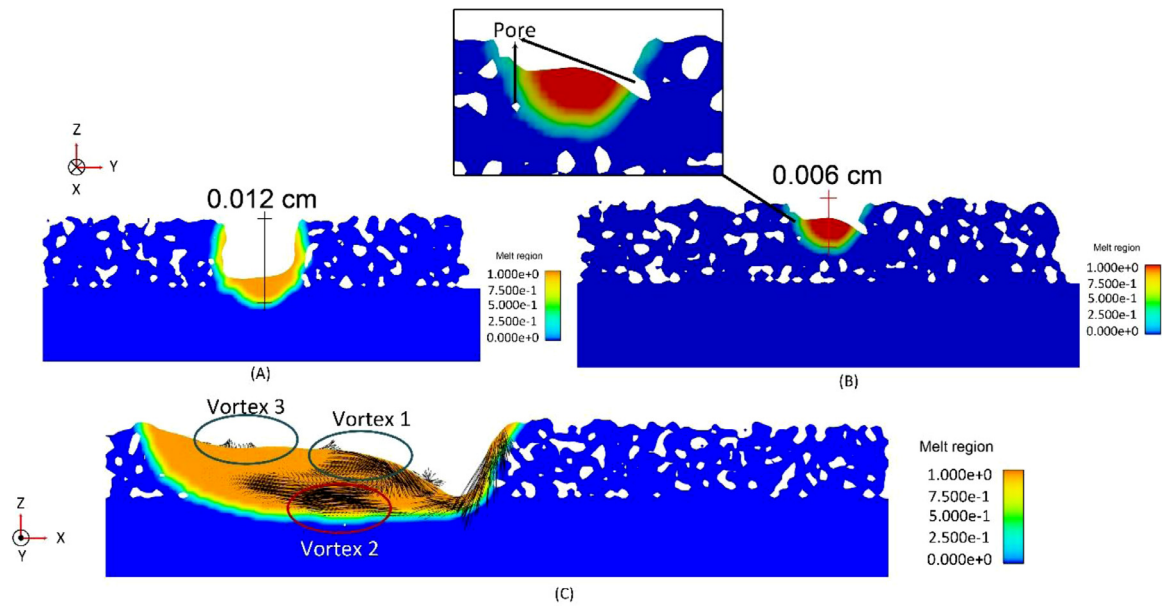
Fig. 12. Melt region temperature (K) and laser track depth for (A) Test Case 10, LP/SS = 0.414 and (B) Test Case 1, LP/SS = 0.212, (C) Z-Cross-Section for Test Case 10 indicating vortices.
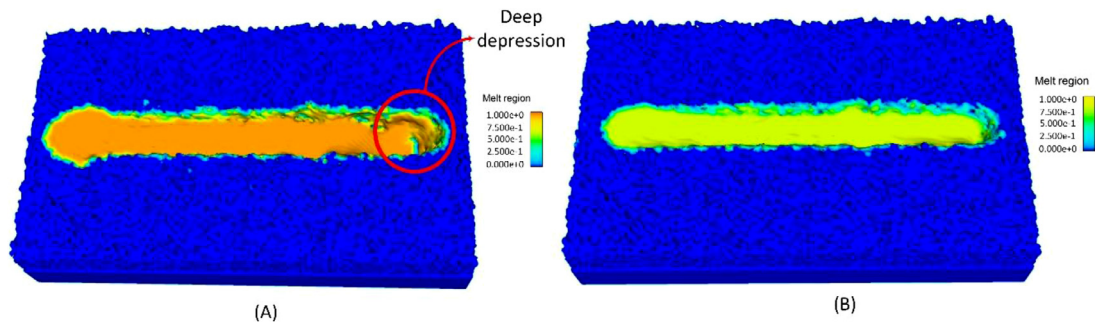
Fig. 13. Deep depression for (A) Test Case 10 versus (B) Test Case 1.
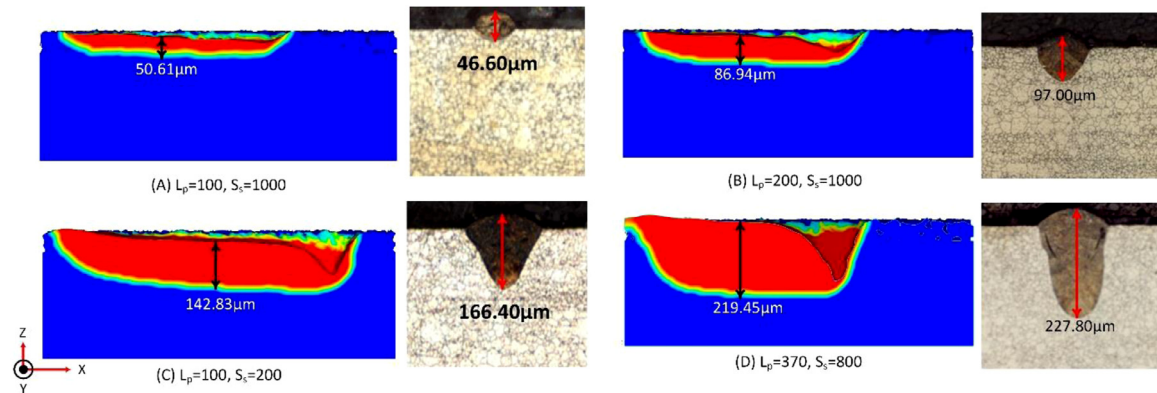

Fig. 14. Y-Cross-section for simulated and experimental melt-tracks with different process parameters (A) Lp=100 W, Ss=1000 mm/s, (B) Lp=200 W, Ss=1000 mm/s, (C) Lp=100 W, Ss=200 mm/s and (D) Lp=370 W, Ss=800 mm/s.

obtained 10.3%, 13.9% respectively which demonstrates an acceptable accuracy and reliability.

6. Conclusion

In this investigation, an analytical model was proposed to estimate meltpool temperature and was verified by numerical DEM simulation of LB-PBF of Inconel 718. Different laser power to scan speed ratios and absorptivity ratios were applied to both models to quantify the accuracy of the numerical and analytical models in the prediction of conduction and keyhole modes. The observed results showed that:

- The analytical model is highly compatible with the numerical model when applied to conduction mode. The difference be-

tween the results of the analytical and simulation models "in conduction mode" was found in the range of 0.54%–6.77%.

- In keyhole mode, the analytical model cannot reliably predict the meltpool temperature. This limitation is assumed to be related in part to the evaporation of chemical compositions of the material during keyhole melting.
- The criteria of energy density to the enthalpy of melting is proposed to distinguish the conduction and keyhole modes. Exceeding this criterion produces a very deep meltpool which can evaporate the material and cause extreme ejection effect and subtracts the material. In contrast, going too far below this criterion may cause a very shallow meltpool and fusion problems.
- The simulation outcomes are compaible with previous observation that recoil force is the primary force for the keyhole mode which drives meltpool features such as depth and pore formation.

This research identifies that the proposed analytical model is a robust tool to predict the meltpool temperature in conduction mode before setting up the machine parameters which can save a considerable amount of time and cost. Therefore, it can provide an effective methodology for initial prediction of acceptable process windows, especially for new materials for which process optimisation data is not readily available.

Future work

Further research will explore the complexities of prediction of meltpool temperature and morphology for keyhole modes. This model should consider a comprehensive phenomenological study of process parameters, keyhole melting physics and non-linear material response to provide predictive capability for both conduction and keyhole modes.

Authorship statement

All persons who meet authorship criteria are listed as authors, and all authors certify that they have participated sufficiently in the work to take public responsibility for the content, including participation in the concept, design, analysis, writing, or revision of the manuscript. Furthermore, each author certifies that this material or similar material has not been and will not be submitted to or published in any other publication before its appearance in the **International journal of heat and mass transfer**.

Dr. Mahyar khorasani, Conceptualization, Methodology, Software, Formal analysis, Writing-Original Draft.

Mr. Amir Hossein Ghasemi, Formal analysis, Resources.

Prof. Martin Leary, Writing - Review & Editing, Methodology, Formal analysis.

Prof. William O'Neil, Writing - Review & Editing, Formal analysis.

Prof. Ian Gibson, Writing - Review & Editing, Methodology, Formal analysis.

Dr. Laura Cordova, Writing - Review & Editing.

Prof. Bernard Rolfe, Writing - Review & Editing, Methodology, Formal analysis.

Declaration of competing interest

The authors confirm that no conflict of interest exists. All authors approved the paper.

Appendix

Tables A1,A2,A3,A4,A5,A6,A7

Table A1
Heat transfare equatiuons.

Equation
$-(\frac{\partial q_x}{\partial x} + \frac{\partial q_y}{\partial y} + \frac{\partial q_z}{\partial z}) + Q = \rho c \frac{\partial T}{\partial t}$
$q_x = -k\frac{\partial T}{\partial x}$
$q_y = -k\frac{\partial T}{\partial y}$
$q_z = -k\frac{\partial T}{\partial z}$

Table A2
Finite Element Solver formulation.

Equation
$[C]\{\dot{T}\} = [K_c]\{T\} = \{R_Q\}$
$C = \int \rho N^T c N dV$
$[K_c] = \int B^T k B dV$
$R_Q = \int Q N^T dV$
$\{T_{n+1}\} = \{T_n\} + \Delta t\{(1-\beta)\{\dot{T}_n\} + \beta\{\dot{T}_{n+1}\}\}$
$(\frac{1}{\beta\Delta t}[C] + [K])\{T_{n+1}\} = R_Q + [C](\frac{1}{\beta\Delta t}\{T_n\} + \frac{1-\beta}{\beta}\{\dot{T}_n\})$

Table A3
Energy conservation and heat source.

Equation
$\frac{\partial\{\rho h\}}{\partial t} + \nabla.\{\rho h u\} - \nabla.\{\lambda\nabla T\} = \{\dot{q}_L\} - \{\dot{q}_r\}$
$\dot{q}_L = -\frac{d\varphi}{dz} = \alpha\varphi = \varphi_{z=0}\alpha \exp(-\int_0^z \alpha\ dt)$
$\varphi_{r,z=0} = (1-R)\frac{2P}{\pi R_L^2}\exp(-\frac{2r^2}{R_L^2})$
$\dot{q}_L(r,z) = (1-R)\frac{2P}{\pi R_L^2}\exp(-\frac{2r^2}{R_L^2})\alpha \exp(-\int_0^z \alpha\ dt)$
$\dot{q}_r = \delta\varepsilon_r\sigma(T^4 - T_0^4)$

Table A4
Momentum conservation.

Equation
$\{\rho\}(\frac{\partial\{u\}}{\partial t} + (\{u\}.\nabla)\{u\} - \nabla.\{\underline{\sigma}\} = f_s + \{\rho\}g$
$\underline{\sigma} = \underline{s} - p\underline{I}$ $\underline{s} = 2\mu(\underline{\dot{\varepsilon}} - \frac{1}{3}tr(\underline{\underline{\dot{\varepsilon}}})\underline{I})$
$tr(\underline{\dot{\varepsilon}}) = \nabla.\{u\}$
$f_s = \gamma\kappa n$
$\kappa n = \nabla_s.\nabla_s\underline{X}$

Table A5

Mass conservation.

Equation
$\nabla.\langle\boldsymbol{u}\rangle^{D_i} = -\frac{1}{\langle\rho\rangle^{D_i}}(\frac{\partial\langle\rho\rangle^{D_i}}{\partial t} + \langle\rho\rangle^{D_i}.\langle\boldsymbol{u}\rangle^{D_i})$
$\nabla.\{\boldsymbol{u}\} = \nabla.((1-\boldsymbol{H})\langle\boldsymbol{u}\rangle^{D_1} + \boldsymbol{H}\langle\boldsymbol{u}\rangle^{D_2} = (1-\boldsymbol{H})\nabla.\langle\boldsymbol{u}\rangle^{D_1} + \boldsymbol{H}\nabla.\langle\boldsymbol{u}\rangle^{D_2} + \nabla\boldsymbol{H}.(\langle\boldsymbol{u}\rangle^{D_2} - \langle\boldsymbol{u}\rangle^{D_1}) = -\frac{(1-\boldsymbol{H})}{\langle\rho\rangle^{D_1}}(\frac{\partial\langle\rho\rangle^{D_1}}{\partial t} + \langle\rho\rangle^{D_1}.\langle\boldsymbol{u}\rangle^{D_1}) - \delta(\langle\boldsymbol{u}\rangle^{D_2} - \langle\boldsymbol{u}\rangle^{D_1}).\boldsymbol{n}_{LS}$
$\delta(\langle\boldsymbol{u}\rangle^{D_2} - \langle\boldsymbol{u}\rangle^{D_1}).\boldsymbol{n}_{LS} = \frac{1}{4\langle\rho\rangle^{D_1}}\frac{\partial\langle\rho\rangle^{D_1}}{\partial t}\boldsymbol{cos}^2(\frac{\pi\psi}{2\epsilon})$

Table A6

Shrinkage.

Equation
$\dot{\boldsymbol{\theta}} = \nabla.\{\boldsymbol{u}\} = -\frac{(1-\boldsymbol{H})}{\langle\rho\rangle^{D_1}}(\frac{\partial\langle\rho\rangle^{D_1}}{\partial t} + \langle\rho\rangle^{D_1}.\langle\boldsymbol{u}\rangle^{D_1}) - \frac{1}{4\langle\rho\rangle^{D_1}}\frac{\partial\langle\rho\rangle^{D_1}}{\partial t}\boldsymbol{cos}^2(\frac{\pi\psi}{2\epsilon})$

Table A7

Evaporation pressure.

Equation
$\boldsymbol{Ps} = \boldsymbol{A}\,\boldsymbol{exp}\{\boldsymbol{B}(1 - \frac{T_\psi}{T})\}$
$\boldsymbol{A} = \frac{RSIZE}{2\pi}\sqrt{\frac{T_\psi}{T}}\boldsymbol{P}_\nu$
$\boldsymbol{B} = \frac{1}{T_{EXP}}\frac{1}{T_\nu}$
$\sqrt{\frac{T_\psi}{T}} \simeq 1$
$\boldsymbol{T_{EXP}} = (\boldsymbol{\gamma} - 1)\frac{c_\nu}{\Delta H_\nu}$

References

[1] I. Gibson, et al., Additive Manufacturing Technologies, 3rd ed., Springer, 2021.

[2] ASTM InternationalISO/ASTM52900-15, Standard Terminology for Additive Manufacturing – General Principles – Terminology, ASTM International, West Conshohocken, PA, 2015.

[3] H. Gu, et al., Multi-physics modelling of molten pool development and track formation in multi-track, multi-layer and multi-material selective laser melting, Int. J. Heat Mass Transf. 151 (2020) 119458.

[4] K.Q. Le, et al., Discontinuity of overhanging melt track in selective laser melting process, Int. J. Heat Mass Transf. 162 (2020) 120284.

[5] T.F. Flint, et al., A thermal fluid dynamics framework applied to multi-component substrates experiencing fusion and vaporisation state transitions, Commun. Phys. 3 (1) (2020) 1–12.

[6] S. Shrestha, Y.Kevin Chou, A numerical study on the keyhole formation during laser powder bed fusion process, J. Manuf. Sci. Eng. 141 (10) (2019).

[7] S. Shrestha, K. Chou, Mesoscopic simulation model to predict temperature distribution and melt Pool size during selective laser scanning, International Manufacturing Science and Engineering Conference, American Society of Mechanical Engineers, 2018.

[8] H. Wang, Y. Zou, Microscale interaction between laser and metal powder in powder-bed additive manufacturing: conduction mode versus keyhole mode, Int. J. Heat Mass Transf. 142 (2019) 118473.

[9] A. Queva, et al., Numerical study of the impact of vaporisation on melt pool dynamics in laser powder bed fusion-application to IN718 and Ti-6Al-4V, Addit. Manuf. (2020) 101249.

[10] Y.-.C. Wu, et al., Parametric study of surface morphology for selective laser melting on Ti6Al4V powder bed with numerical and experimental methods, Int. J. Mater. Form. 11 (6) (2018) 807–813.

[11] S. Shrestha, S. Rauniyar, K. Chou, Thermo-fluid modeling of selective laser melting: single-track formation incorporating metallic powder, J. Mater. Eng. Perform. 28 (2) (2019) 611–619.

[12] S.A. Khairallah, et al., Laser powder-bed fusion additive manufacturing: physics of complex melt flow and formation mechanisms of pores, spatter, and denudation zones, Acta Mater. 108 (2016) 36–45.

[13] W.E. King, et al., Observation of keyhole-mode laser melting in laser powder-bed fusion additive manufacturing, J. Mater. Process. Technol. 214 (12) (2014) 2915–2925.

[14] R.K. Ganeriwala, et al., Evaluation of a thermomechanical model for prediction of residual stress during laser powder bed fusion of Ti-6Al-4V, Addit. Manuf. 27 (2019) 489–502.

[15] G. Tapia, et al., Gaussian process-based surrogate modeling framework for process planning in laser powder-bed fusion additive manufacturing of 316L stainless steel, Int. J. Adv. Manuf. Technol. 94 (9–12) (2018) 3591–3603.

[16] W. King, et al., Overview of modelling and simulation of metal powder bed fusion process at Lawrence Livermore National Laboratory, Mater. Sci. Technol. 31 (8) (2015) 957–968.

[17] P.S. Cook, A.B. Murphy, Simulation of melt pool behaviour during additive manufacturing: underlying physics and progress, Addit. Manuf. 31 (2020) 100909.

[18] F. Dausinger, J. Shen, Energy coupling efficiency in laser surface treatment, ISIJ Int. 33 (9) (1993) 925–933.

[19] K.C. Mills, Recommended Values of Thermophysical Properties For Selected Commercial Alloys, Woodhead Publishing, 2002.

[20] Y. Zhao, et al., Isothermal $\gamma \to \varepsilon$ phase transformation behavior in a Co-Cr-Mo alloy depending on thermal history during electron beam powder-bed additive manufacturing, J. Mater. Sci. Technol. (2020).

[21] Y. Zhao, et al., Significance of powder feedstock characteristics in defect suppression of additively manufactured Inconel 718, Addit. Manuf. (2020) 101277.

[22] X. Gao, et al., Numerical analysis of non-spherical particle effect on molten pool dynamics in laser-powder bed fusion additive manufacturing, Comput. Mater. Sci. 179 (2020) 109648.

[23] Y. Zhao, et al., Role of operating and environmental conditions in determining molten pool dynamics during electron beam melting and selective laser melting, Addit. Manuf. 36 (2020) 101559.

[24] I. Gibson, et al., Software for additive manufacturing, in: Additive Manufacturing Technologies, Springer, Cham, 2021, pp. 491–524.

[25] C. Qiu, et al., On the role of melt flow into the surface structure and porosity development during selective laser melting, Acta Mater. 96 (2015) 72–79.

[26] C. Panwisawas, et al., Keyhole formation and thermal fluid flow-induced porosity during laser fusion welding in titanium alloys: experimental and modelling, Acta Mater. 126 (2017) 251–263.

[27] Y. Lu, Y. Wang, P.F. Mendez, Width of thermal features induced by a 2-D moving heat source, Int. J. Heat Mass Transf. 156 (2020) 119793.

[28] C. Katinas, Y.C. Shin, Prediction of initial transient behavior with stationary heating during laser powder bed fusion processes, Int. J. Heat Mass Transf. 153 (2020) 119663.

[29] Bayat, M., et al., A fundamental investigation of thermo-capillarity in laser powder bed fusion of metals and alloys.Int. J. Heat Mass Transf.. 166: p. 120766.

[30] H. Wang, Y. Zhang, K. Chen, Modeling of temperature distribution in laser welding of lapped martensitic steel M1500 and softening estimation, J. Manuf. Sci. Eng. (11) (2016) 138.

[31] S.J. Wolff, et al., Experimentally validated predictions of thermal history and microhardness in laser-deposited Inconel 718 on carbon steel, Addit. Manuf. 27 (2019) 540–551.

[32] W. Yan, et al., Meso-scale modeling of multiple-layer fabrication process in selective electron beam melting: inter-layer/track voids formation, Mater. Des. 141 (2018) 210–219.

[33] S. Katayama, Introduction: fundamentals of laser welding, in: S. Katayama (Ed.), Handbook of Laser Welding Technologies, Woodhead Publishing, 2013, pp. 3–16.

[34] H. Rastan, et al., Heat transfer study of enhanced additively manufactured minichannel heat exchangers, Int. J. Heat Mass Transf. 161 (2020) 120271.

[35] A.M. Khorasani, I. Gibson, A.R. Ghaderi, Rheological characterization of process parameters influence on surface quality of Ti-6Al-4V parts manufactured by selective laser melting, Int. J. Adv. Manuf. Technol. 97 (9–12) (2018) 3761–3775.

[36] I. Gibson, et al., Powder bed fusion, in: Additive Manufacturing Technologies, Springer, Cham, 2021, pp. 125–170.

[37] B. Schoinochoritis, D. Chantzis, K. Salonitis, Simulation of metallic powder bed additive manufacturing processes with the finite element method: a critical review, Proc. Inst. Mech. Eng., Part B 231 (1) (2017) 96–117.

[38] R. Rai, et al., Heat transfer and fluid flow during keyhole mode laser welding of tantalum, Ti–6Al–4V, 304L stainless steel and vanadium, J. Phys. D. Appl. Phys. 40 (18) (2007) 5753.

[39] I. Yadroitsev, et al., Use of track/layer morphology to develop functional parts by selective laser melting, J. Laser Appl. 25 (5) (2013) 052003.

[40] D. Hann, J. Iammi, J. Folkes, A simple methodology for predicting laser-weld properties from material and laser parameters, J. Phys. D Appl. Phys. 44 (44) (2011) 445401.